Optimization of the HOVF Spray Parameters by Taguchi Method for High Corrosion-Resistant Fe-Based Coatings

Yujiao Qin, Yuping Wu, Jianfeng Zhang, Sheng Hong, Wenmin Guo, Liyan Chen, and Hao Liu

Taguchi method was used to optimize the parameters of the high velocity oxygen fuel (HVOF) spray process and obtain the high corrosion-resistant Fe-based coatings. Based on the signal-to-noise (S/N) ratio and the analysis of variance, the significance of spray parameters in determining the porosity of the coatings was found to be in the order of spray distance, oxygen flow, and kerosene flow. Thus, the optimal parameters for the porosity of the HVOF sprayed Fe-based coating were determined as 280 mm for the spray distance, 963 scfh for the oxygen flow, and 28 gph for the kerosene flow. The potentiodynamic polarization and EIS tests indicated that the Fe-based coating prepared with the optimal parameters exhibited a higher corrosion potential (E_{corr}) of -196.14 mV, a lower corrosion current density (i_{corr}) of 0.14 µA/cm^2, and a higher coating resistance (R_c) of 2.26×10^6 Ω cm^2 than those of the hard chromium coating in 3.5% sodium chloride solution. This superior corrosion resistance could be attributed to the dense structure with low porosity and partially amorphous phases of the Fe-based coatings.

1. Introduction

Corrosion is one of the major problems in engineering applications by causing great injuries and enormous economy lost (Ref 1-3). Therefore, the high corrosion-resistant coatings deposited on the surface of components by various thermal spray technologies have been explored to solve this problem (Ref 4-9). Among those widely used thermal spray technologies, high velocity oxygen fuel (HVOF) is taken as a competitive one due to its unique advantages (Ref 10-12). The most important is that, during HVOF spraying, the feedstock powders will be injected into a high velocity hot jet, which is generated through combustion of a fuel (mostly using kerosene) and oxygen with a desired mass ratio, and thus a dense coating with low porosity and few oxides could be produced.

On the other hand, the cost-effective Fe-based alloy coatings, especially Fe-based amorphous/Nanocrystalline ones, have shown promising applications in severe corrosive environments, and replacement of hard chromium coatings in some special applications (Ref 4, 13-15). Many studies have been made to investigate the engineering performance, especially the corrosion resistance of HVOF sprayed Fe-based alloy coatings. Bakare et al. (Ref 4) prepared HVOF sprayed FeCrMoCB amorphous coating, which showed better corrosion resistance than that of its crystalline form in 0.5 mol/L sulfuric acid solution and 3.5% sodium chloride electrolytes. Farmer et al.

(Ref 16) studied the corrosion resistance of Fe-based amorphous coating prepared by HVOF and found that the coating exhibited a very good corrosion resistance in simulated groundwater. Guo et al. found that the HVOF sprayed $Fe_{49.7}Cr_{18}Mn_{1.9}Mo_{7.4}W_{1.6}B_{15.2}C_{3.8}Si_{2.4}$ amorphous coating showed good corrosion resistance in 3.5% sodium chloride solution (Ref 17). Overall, it could be concluded that the elevated corrosion resistance could be usually attributed to the appropriate microstructures, such as the low porosity, the amorphous phases, and the compact bonding of the coating with the substrate.

Furthermore, the spray parameters in HVOF spray process also have a significant influence on the microstructures and then corrosion resistance of the coatings (Ref 18-20). Zhou et.al (Ref 21) indicated that the porosity and amorphous fraction of the $Fe_{48}Cr_{15}Mo_{14}C_{15}B_6Y_2$ amorphous coating decreased as the kerosene and oxygen flow increase within the parameter range examined. Wang et al. (Ref 22) found the FeCrMoMnWBCSi amorphous metallic coatings obtained with the oxygen/fuel ratio of 4.2 and the powder feed rate of 40 g/min by HVOF spray process exhibiting the best corrosion resistance in 1 wt.% sodium chloride solution. In addition to the spray parameters stated above, flow rate, powder size distribution, and spray distance also play a crucial role in the manufacturing and quality of coating (Ref 18-22). Although many researchers have studied the effect of HVOF spray parameters on the coating properties, it is hard to make consistent conclusions since different spray parameters are focused by researchers. It is necessary to make further investigation of spray parameters during HVOF process in preparing Fe-based alloy coatings.

Taguchi method (Ref 23) is a powerful approach to investigate the effects of multiple factors on performance in a simple, an efficient, and a systematic way. In recent years, numerous applications of the Taguchi method have been seen in the preparation of other materials and coatings (Ref 19, 24, 25). However, the application of the method in Fe-based coatings is still limited.

In this study, the main objective is to apply the Taguchi design method on optimization of spray parameters of HVOF

Yujiao Qin, Yuping Wu, Jianfeng Zhang, Sheng Hong, Wenmin Guo, Liyan Chen and **Hao Liu**, Institute of Metals and Protection, College of Mechanics and Materials, Hohai University, 1 Xikang Road, Nanjing 210098 Jiangsu, China. Contact e-mails: wuyuping@hhu.edu.cn, wuyphhu@163.com, and jfzhang@hhu.edu.cn.

sprayed Fe-based alloy coatings applied to achieve the lowest porosity, as well as to study the corrosion performance of coating with optimal spray parameters in 3.5% sodium chloride solution.

2. Experimental Procedure

2.1 Preparation of the Coating

The commercial Fe-based alloy powder was used with a chemical composition of a (28.0-32.0 wt.% Cr, 17.0-21.5 wt.% Ni, 8.4-11.0 wt.% Co, 3.3-4.5 wt.% Mo, 3.1-4.0 wt.% B, 2.0-3.0 wt.% Cu, 1.0-1.6 wt.% Si, 0.12 max wt.% C, 0.02 max wt.% S, and the balance Fe) and a particle size of 15-45 μm. The stainless steel (1Cr18Ni9Ti) plates served as substrate with a dimension of 35 mm × 35 mm × 6 mm. It was machined and polished, then degreased by acetone, dried in air, and grit-blasted for spraying by a Tafa-JP5000 system.

In this study, the spray parameters of spray distance, oxygen flow, and kerosene flow will be investigated. At the point of impacting on the substrate, the characteristics of the in-flight particles, such as the velocity, temperature, degree of melting, and the oxide content, were strongly influenced by the optimization of spray parameters, including spray distance, oxygen flow, and kerosene flow. With the increase of spray distance, both the temperature and velocity of the in-flight particles will decrease, thus increasing the volume fraction of unmelted particles and oxidation products. When the oxygen flow increases, the fuel is combusted more completely, resulting in particles with higher temperature and enough kinetic energy. However, much higher oxygen flow can also lead to the oxidation of the particles. The increase of kerosene flow will result in the large amount of unmelted particles. Thus, the three spray parameters of spray distance, oxygen flow, and kerosene flow are selected as shown in Table 1. Then the Taguchi method based on a L_9 orthogonal array with four columns and nine rows was used. Each parameter was assigned to a column, nine spray parameter combinations being available. Since the L_9 orthogonal array had four columns, one column of the array was left empty for the error of the experiments. Therefore, the number of experiments to be conducted was reduced to 9 as shown in Table 2. Other parameters were employed at an argon carrier gas flow rate of 23 scfh, a powder feed rate of 5 rpm, and a spray gun traverse velocity of 600 mm/s.

2.2 Characterization of the Coatings

The phase composition of the powder and coating was investigated by x-ray diffraction (XRD, Bruker D8-Advanced, Germany) with a copper Ka radiation. The microstructure of the as-sprayed coating was observed by scanning electron micro-scope (SEM, Hitachi S-3400N, Japan). Selected area electron diffraction (SAED) pattern and finer-scale microstructural characterization of the coating were performed using a transmission electron microscope (TEM, JEM-2000EX, Japan) operated at 200 kV. The porosity of the coatings was calculated through OLYMPUS-BX51M optical microscope combined with DT-2000 image analysis software. Fifteen measurements were averaged for each reported value to ensure the reliability.

The porosity of the coating will be used as the optimizing criterion in the Taguchi method in order to achieve the lowest porosity, as well as the best corrosion resistance. Many researchers demonstrated the relationship between the porosity of the thermal sprayed coatings and the corrosion resistance. The lower the porosity, the better the corrosion resistance (Ref 20, 21, 26, 27). Zhou et al. (Ref 21) found that the corrosion resistance of the Fe-based amorphous metallic coating by HVOF thermal spraying increases evidently when the porosity decreases from 1.89 to 1.22% due to the elimination of through pores. Wang et.al (Ref 26) demonstrated that the corrosion resistance of Fe-based amorphous coating increased after sealing treatments.

The corrosion behaviors of the coatings and hard chromium coating were evaluated by electrochemical measurement on a Parstat 2273 electrochemical site. Prior to the electrochemical measurements, the specimens were cold mounted using epoxy resin, prepared by sequential grinding with 240-2000 mesh grade silicon carbide abrasive papers, polished by 2.5 and 0.5 μm diamond pastes, and then degreased in acetone by ultrasonic bath and dried in air. Electrochemical measurements were performed with a standard three-electrode system using a platinum counter electrode (with exposed area of 1.2 mm^2) and saturate calomel reference electrode. The specimen served as the working electrode with the area of only 1 cm^2 exposed. All experiments were carried out in 3.5% sodium chloride solution at 298 K. The experiments were conducted after being immersed for 1 h and the open-circuit potential (OCP) became almost steady. Potentiodynamic polarization swept from −0.25 to +1.5 V relative to the open-circuit potential at a fixed rate of 1 mV/s. Electrochemical impedance spectroscopy (EIS) measurements were performed using a sinusoidal potential perturbation of 10 mV in a frequency range of 10 kHz to 10 mHz. The good reproducibility was ensured by repeating each test twice.

Table 1   Spray parameters and levels used in this experiment

Symbol	Spray parameter	Level		
		1	2	3
A	Spray distance, mm	280	330	380
B	Oxygen flow, scfh	1850	2049	2251
C	Kerosene flow, gph	5.8	6.2	6.6

Table 2   Experimental layout using an L9 orthogonal array

Experiment no.	Spray parameter level			
	A (spray distance)	B (oxygen flow)	C (kerosene flow)	D (error)
1	A1	B1	C1	D1
2	A1	B2	C2	D2
3	A1	B3	C3	D3
4	A2	B1	C2	D3
5	A2	B2	C3	D1
6	A2	B3	C1	D2
7	A3	B1	C3	D2
8	A3	B2	C1	D3
9	A3	B3	C2	D1

3. Results and Discussion

3.1 Analysis of the Signal-to-Noise Ratio

The signal-to-noise (S/N) ratio is usually used in the Taguchi method to measure the performance characteristic deviating from the desired value (Ref 11, 19, 24, 25). The S/N ratio (η) is defined as

$$\eta = -10 \log(MSD), \tag{Eq 1}$$

where MSD is the mean-square deviation for the output characteristic. The MSD is different according to the category of characteristic. There are three categories of performance characteristics, that is, the nominal-the-better, the higher-the-better, and the lower-the-better. Regardless of the category of the performance characteristic, the larger S/N ratio corresponds to the better performance characteristic. Therefore, the optimal level of the spray parameters is the level with the highest S/N ratio (η). The aim of this paper is to prepare coatings with better corrosion resistance. Lower porosity represents a higher corrosion resistance of the coating (Ref 22). Thus, the lower-the-better performance characteristic for porosity should be implemented to obtain optimal corrosion resistance performance. The MSD for the lower-the-better performance characteristic can be expressed as

$$MSD = \frac{1}{n} \sum_{i=1}^{n} P_i^2, \tag{Eq 2}$$

where n is the replication number of the experiment and P_i is the value of porosity for the ith test.

The experimental results for porosity and the corresponding S/N ratio calculated by Eq 1 and 2 are exhibited in Table 3. Since the experimental design is orthogonal, it is then possible to separate out the effect of each spray parameter at different levels. In the L_9 orthogonal array of Table 3, spraying condition could be optimum as 6.375 S/N ratio for porosity.

The S/N response table for porosity is shown in Table 4, which presents the calculated mean S/N ratio for each level of the spray parameters. The spray parameter that has the strongest influence is also determined depending on the value of Δ (delta) as shown in Table 4. Delta equals the difference between maximum and minimum S/N ratios for a particular spray parameter. The higher the value of delta, the more influential is the spray parameter. It can be seen that the strongest influence is exerted by the spray distance and the oxygen flow, which have the highest values of delta, 4.579 and 2.025 dB, respectively.

Figure 1 shows the mean S/N response plot for porosity. The plot shows the variation of S/N ratio as the spray parameters changed from one level to another. The larger is the S/N ratio, the lower is the porosity. It can be suggested that the optimal spray parameter for porosity is the combination of A1, B2, and C2. It is evident from Fig. 1 that the spray distance has the greatest increasing effect on the porosity. With the increase of spray distance, both the temperature and velocity of the in-flight
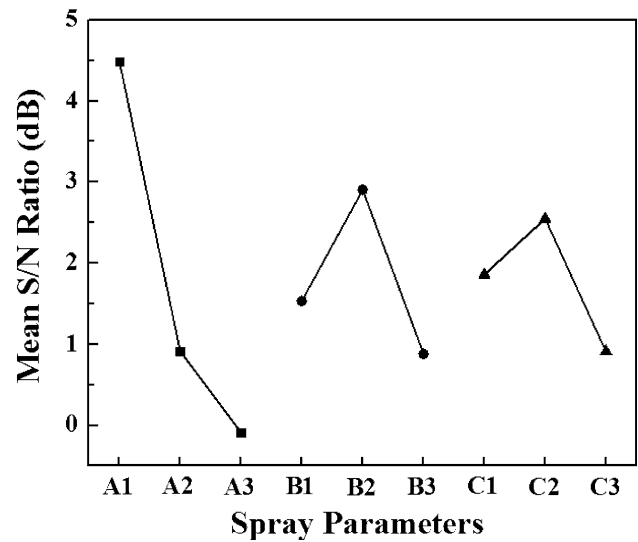

Fig. 1 The mean S/N graph for porosity

Table 3 Experimental results for porosity and corresponding S/N ratio

Experiment no.	Spray distance, mm	Oxygen flow, scfh	Kerosene flow, gph	Porosity, %	S/N ratio, dB
1	280	1850	5.8	0.64	3.876
2	280	2049	6.2	0.48	6.375
3	280	2251	6.6	0.69	3.223
4	330	1850	6.2	0.80	1.938
5	330	2049	6.6	0.92	0.724
6	330	2251	5.8	0.99	0.087
7	380	1850	6.6	1.15	−1.214
8	380	2049	5.8	0.83	1.618
9	380	2251	6.2	1.08	−0.668

Table 4 S/N response table for porosity

Symbol	Spray parameter	Mean S/N ratio, dB			
		Level 1	Level 2	Level 3	Δ (max − min)
A	Spray distance	4.491	0.916	−0.088	4.579
B	Oxygen flow	1.533	2.906	0.881	2.025
C	Kerosene flow	1.860	2.548	0.911	1.637

particles will decrease, thus increasing the volume fraction of unmelted particles and oxidation products. As a result, a coating with higher porosity will be produced, which is similar to the conclusion obtained by other researchers (Ref 28, 29). As for the oxygen flow and kerosene flow, the porosity of the coating first decreases and then increases with the level of spray parameters increased. With the increase of oxygen flow, the fuel is combusted more completely, resulting in particles with higher temperature and enough kinetic energy. However, much higher oxygen flow can also lead to the oxidation of the particles, since the completely melted particles exposed to the high temperature atmosphere will react with oxygen further (Ref 22). Therefore, the porosity of the coating can be decreased with a proper proportion of oxygen flow and kerosene flow, and thus a much denser microstructure coating can be obtained.

3.2 Analysis of Variance

The purpose of the analysis of variance (ANOVA) is used to investigate which spray parameters significantly affect the porosity. This is accomplished by separating the total variability of the S/N ratios into contributions by each of the spray parameters and the errors. The total variability of the S/N ratio is measured by the sum of the squared deviations from the total mean S/N ratio. Then the Fisher's values (F) are calculated for each spray parameters. Usually, if $F > 4$, the related spray parameter has a significant effect on the performance characteristic. If the F value for a factor is below 4, it means that this factor is not significant and can be neglected (Ref 30).

Table 5 shows the results of ANOVA for porosity. It can be found that the spray distance and the oxygen flow are the significant factors in affecting porosity with 74.63 and 13.76% contributions, respectively, while the kerosene flow is the insignificant factor with 8.71% contribution. It has been demonstrated that the spray distance is a significant variable in determining the porosity of the coatings. Therefore, based on the S/N ratio and ANOVA analyses, the optimum conditions are the spray distance at level 1, the oxygen flow at level 2, and the kerosene flow at level 2. In other words, the optimal parameters under the same condition for the porosity of the Fe-based alloy coating according to the range of spray parameter provided in the paper are 280 mm for the spray distance, 963 scfh for the oxygen flow, and 28 gph for the kerosene flow. Moreover, the No. 2 Fe-based alloy coating was just prepared with the optimal spray parameters.

3.3 Microstructural Characterization

The x-ray diffraction pattern of Fe-based alloy coating is shown in Fig. 2. It can be seen from the pattern that the coating exhibits a broad halo peak at $2\theta = 40°$-$50°$ which overlaps with a small amount of crystalline diffraction peaks. The broad halo peak indicates the existence of amorphous phase, which is similar to the results showed in other researches (Ref 14-16). The major crystalline phases in the coatings are composed of α-Fe (Cr) solid solution and some types of borides, including CrB, FeB, Cr_2B, Fe_2B, and Ni_2B.

In order to obtain detailed microstructural information, TEM was undertaken at a finer scale of Fe-based alloy coating. Figure 3 shows the TEM image of the coating. The diffused halo ring in the SAED pattern (inset of Fig. 3) confirms the formation of amorphous phase. As shown in Fig. 3, the coating consists of amorphous phase, crystalline phases, and some crystalline phases were embedded in the amorphous matrix. These diffuse characters seen in the TEM agree with the XRD results noted in Fig. 2. The formation of the amorphous phase is probably due to the high cooling rate during the HVOF spray process and the proper powder composition (Ref 14).

Figure 4 presents the typical morphology on the cross section of the optimized coating (No. 2 Fe-based coating, Fig. 4a) and No. 7 Fe-based coating (Fig. 4b) prepared by different spray parameters. It is evident that the No. 2 coating shows a very dense structure with porosity of 0.48%, few unmelted or half-melted particles, and compact bonding with the substrate. While compared to the optimized coating, the No. 7 coating exhibits much more small pores with a porosity of 1.15%.

3.4 Electrochemical Corrosion Behavior

The coatings of Nos. 2 and 7, with the lowest and highest porosity of 0.48% and 1.15% separately (Table 3), were selected for comparison of the corrosion resistance in a 3.5%
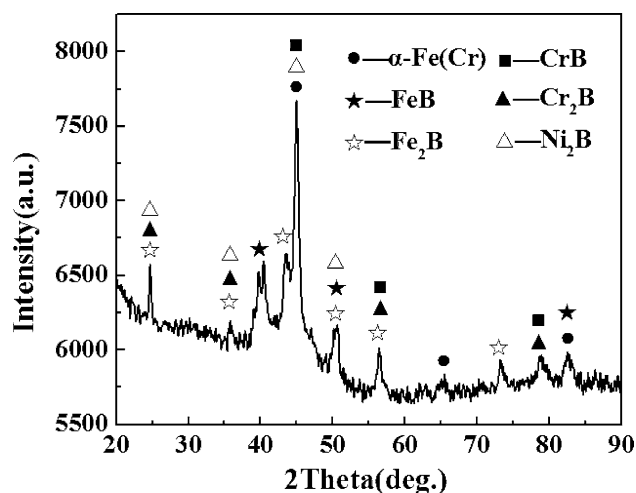

Fig. 2 XRD patterns of the Fe-based alloy coating

Table 5 Results of the AVONA for porosity

Symbol	Spray parameter	Sum of square, S	Degrees of freedom	Variance, V	F	Contribution, %
A	Spray distance	34.760	2	17.38	25.691	74.63
B	Oxygen flow	6.410	2	3.205	4.738	13.76
C	Kerosene flow	4.055	2	2.0275	2.997	8.71
Error		1.35	2	0.675		2.90
Total		46.575	8			

Fig. 3 TEM images of the Fe-based alloy coating

Fig. 4 The typical morphology on the cross section of the coating prepared by different parameters: (a) No. 2 Fe-based coating and (b) No. 7 Fe-based coating
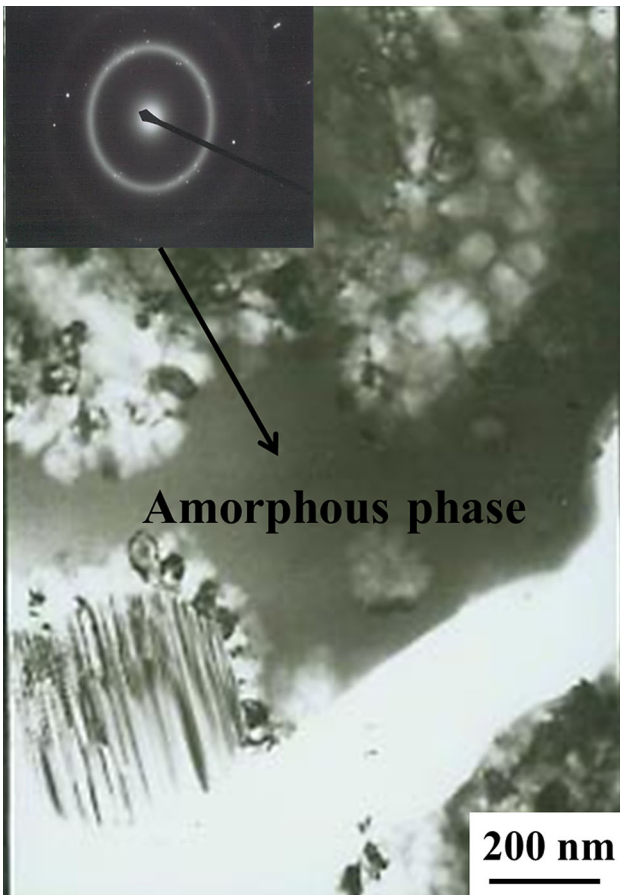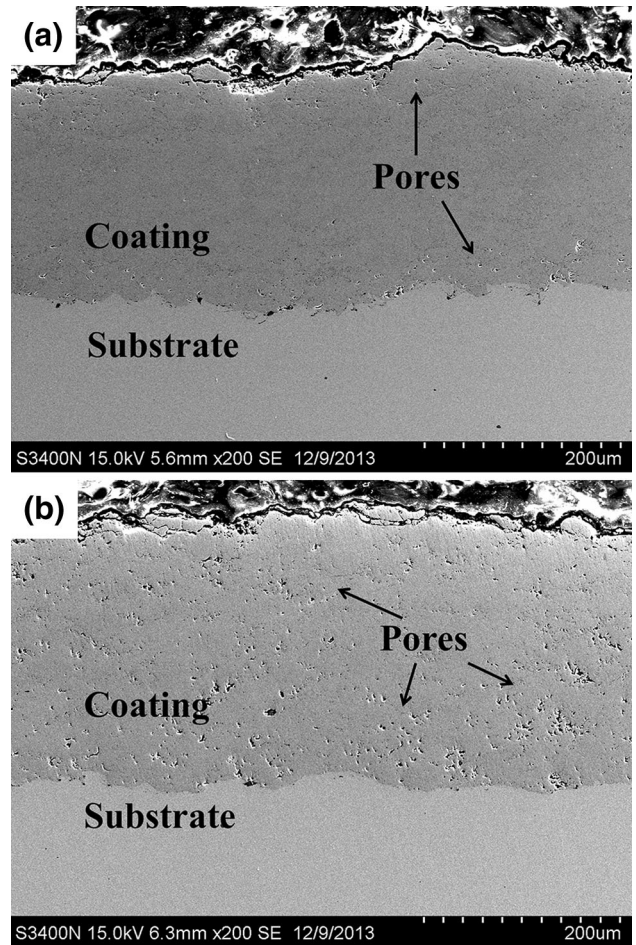
sodium chloride solution. The hard chromium coating was also selected as a reference material.

Figure 5 and Table 6 show the potentiodynamic polarization curves and the calculated values of corrosion potential (E_{corr}) as well as the corrosion current density (i_{corr}) according to the method of the Tafel extrapolation, respectively. The potentiodynamic polarization curves of Fe-based coatings and hard chromium coating exhibited a similar profile, indicating that all of the coatings are obviously spontaneous passivated in the 3.5% sodium chloride solution. The transpassive potentials for the Fe-based and hard chromium coating are higher than 1.0 V, suggesting the high resistance localized corrosion. The passive current density of the No. 2 coating ($\sim 10^{-4}$ A/cm^2) is much lower than that of the No. 7 coating and hard chromium coating. Simultaneously, No. 2 coating also showed a much higher corrosion potential and much lower corrosion current density than those of the No. 7 coating and the hard chromium coating. The superior corrosion resistance of No. 2 coating could be attributed to its dense structure and low porosity. Table 6 shows the electrochemical parameters of the samples from potentiodynamic polarization curves. The corrosion potential (E_{corr}) of the No. 2 coating was higher than that of No. 7 and hard chromium coatings, while the corrosion current density (i_{corr}) was lower than that of the other two coatings. As is known to all, higher corrosion potential exhibits higher chemical stability and lower corrosion tendency. Lower corrosion current density leads to lower corrosion rate (Ref 31). Therefore, No. 2 Fe-based coating has the highest corrosion
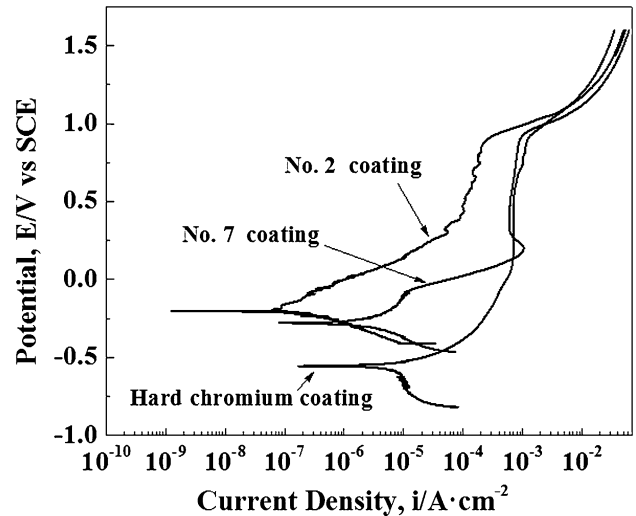

Fig. 5 Potentiodynamic polarization curves of HVOF sprayed Fe-based coatings under different conditions and hard chromium coating in 3.5% sodium chloride solution

potential (E_{corr}) and lowest corrosion current density (i_{corr}), indicating the best corrosion resistance in 3.5% sodium chloride solution.

Table 6 Summary of the electrochemical parameters of the samples from potentiodynamic polarization curves

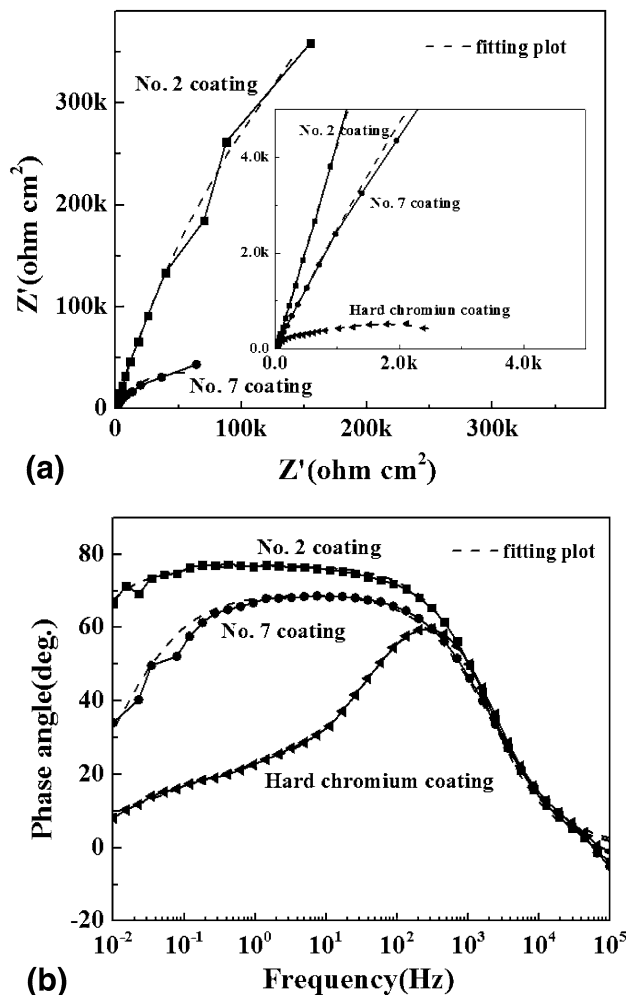| Coatings	E_{corr}, mV	i_{corr}, µA/cm^2	b_c, mV	b_a, mV
No. 2 Fe-based coating	−196.14	0.14	98.61	294.98
No. 7 Fe-based coating	−287.49	5.04	186.58	172.83
Hard chromium coating	−554.35	14.12	223.41	225.63

Fig. 6 The Nyquist diagrams (a) and Bode phase plots (b) of the Fe-based coatings and hard chromium coating in 3.5% sodium chloride solution

Fig. 7 The equivalent circuit representative of the Fe-based coatings and the hard chromium coating

Table 7 Electrochemical parameters obtained from EIS spectra of the Fe-based coatings and hard chromium coating

Coatings	R_s, Ω cm^2	Q_c, µF/cm^2	N_c	R_c, Ω cm^2
No. 2 Fe-based coating	12.19	27.06	0.86	2.26×10^6
No. 7 Fe-based coating	10.24	70.96	0.78	1.05×10^5
Hard chromium coating	12.74	93.28	0.66	2.04×10^3

an enhanced corrosion resistance. The magnitudes of the capacitive loop in the 3.5% sodium chloride solution decrease in the order of the No. 2 Fe-based coating, the No. 7 Fe-based coating, and the hard chromium coating. It indicates the No. 2 Fe-based coating shows the highest corrosion resistance in 3.5% sodium chloride solution.

Based on the above analysis, the equivalent circuit to describe the electrochemical reaction for the Fe-based coating and the hard chromium coating is shown in Fig. 7. It contains the elements of a solution resistance (R_s), a coating resistance (R_c), and a constant phase element CPE-c (Q_c) used to replace capacitance, since there is hardly a pure capacitance in a real electrochemical process. This equivalent circuit has been reported in other Fe-based alloy coating or amorphous/nanocrystalline coating systems (Ref [32-34]) in 3.5% sodium chloride solutions.

The dotted line in Fig. 6 represents the calculated EIS spectra based on the equivalent circuit (Fig. 7), which fit very well the test results for the coatings under most frequencies. The electrochemical parameters extracted from the equivalent circuits (Fig. 7) are summarized in Table 7. The R_c values of the Fe-based coatings are higher than that of the hard chromium coating, indicating the better corrosion resistance of the Fe-based coating. In addition, it is noted that the R_c values of No. 2 Fe-based coating (2.26×10^6 Ω cm^2) is higher than that of the No. 7 Fe-based coating (1.05×10^5 Ω cm^2). All EIS plots agreed well with the results of the potentiodynamic polarization mentioned above (Fig. 5).

Taking the potentialdynamic polarization and EIS tests into consideration, compared to the No. 7 Fe-based coating, the No. 2 Fe-based coating displayed superior corrosion resistance as indicated by a higher corrosion potential, lower corrosion current density, and higher coating resistance (R_c). This phenomenon may be due to the different porosity with different spraying parameters of the two coatings. The absence of pores and microcracks, which are mainly paths for the electrolyte to reach the steel substrate, played an important role in preserving the integrity of the coating. This result also reflected the unfavorable effect of pores existing in the No. 7 Fe-based

In order to evaluate the variation in the electrochemical reactions of the Fe-based coatings and the hard chromium coating, EIS was measured in the 3.5% sodium chloride solution as shown in Fig. 6. Figure 6(a) and (b) show the Nyquist and Bode phase plots of the coatings in 3.5% NaCl solution at OCP, respectively. It can be seen that for each coating there is only one large high frequency capacitive loop on Nyqusit diagram (see the enlargement in the inset of Fig. 6a) and one inflection point on corresponding Bode phase plot (Fig. 6b), indicating that all the coatings exhibited single time constants in the corrosion process. The equivalent circuits based on the different of time constants are selected. This high frequency loop could be physically related to the coating characteristic and a large magnitude of the impedance showed
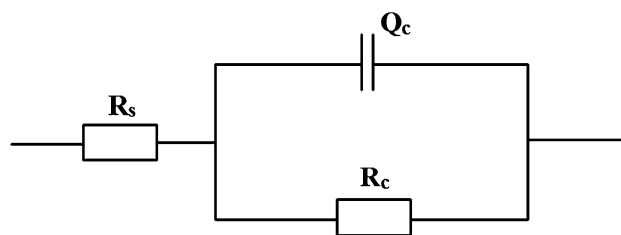
coating on corrosion resistance and the improvement of the corrosion resistance through optimizing the thermal spraying parameters is necessary. In addition, the corrosion resistance of the Fe-based coating is better than that of the hard chromium coating in 3.5% sodium chloride solution. The Fe-based coating fabricated by HVOF technology with a rapidly cooling rate has a very dense structure, low porosity, and partially amorphous phase with less crystalline defects. It is difficult for the aggressive solution to penetrate into the coating and consequently improve the resistance to charge transfer (Ref 26). While due to the existence of a high density of pores and microcracks in the hard chromium coating, the electrolyte penetrates into the coating more easily through such coating defects. Thus, the hard chromium coating could be replaced by the HVOF sprayed Fe-based coatings in some corrosive environments.

4. Conclusion

The spray parameters (spray distance, oxygen flow, and kerosene flow) of HVOF were optimized with the method of Taguchi design on a L_9 orthogonal array to obtain corrosion-resistant Fe-based coatings. The main conclusions are as follows.

(1) Based on the S/N ratio and ANOVA analyses, the spray parameters for the porosity were optimized as 280 mm for the spray distance, 963 scfh for the oxygen flow, and 28 gph for the kerosene flow. The significance of spray parameters in determining the porosity of the coatings was in the order of spray distance, oxygen flow, and oxygen flow.

(2) The coating prepared with the optimal spray parameters (i.e., the No. 2 Fe-based coating) showed a dense structure with a porosity of only 0.48%, few unmelted or half-melted particles, and compact bonding with the substrate. However, the porosity of No. 7 coating exhibits much more small pores with a porosity of 1.15%. The as-prepared coatings were both composed of α-Fe(Cr) solid solution, some types of borides and amorphous phases.

(3) The potentiodynamic polarization and EIS tests in 3.5% sodium chloride solution indicated that the No. 2 Fe-based coating exhibited the highest corrosion potential (E_{corr}) of −196.14 mV, the lowest corrosion current density (i_{corr}) of 0.14 μA/cm^2, and the highest coating resistance (R_c) of 2.26×10^6 Ω cm^2 than those of the No. 7 Fe-based coating and the hard chromium coating. The superior corrosion resistance of the Fe-based coating with the optimal spray parameters could be attributed to the dense structure with low porosity and partially amorphous structure, thus making the replacement of the hard chromium coating possible in some corrosive environments.

Reference

1. J. Guilemany, N. Espallargas, P. Suegama, and A. Benedetti, Comparative Study of Cr$_3$C$_2$-NiCr Coatings Obtained by HVOF and Hard Chromium Coatings, *Corros. Sci.*, 2006, **48**, p 2998-3013
2. J. Kawakita, T. Fukushima, S. Kuroda, and T. Kodama, Corrosion Behaviour of HVOF Sprayed SUS316L Stainless Steel in Seawater, *Corros. Sci.*, 2002, **44**, p 2561-2581
3. J. Flores, A. Neville, N. Kapur, and A. Gnanavelu, Corrosion and Erosion-Corrosion Processes of Metal-Matrix Composites in Slurry Conditions, *J. Mater. Eng. Perform.*, 2012, **21**, p 395-405
4. M. Bakare, K. Voisey, K. Chokethawai, and D. McCartney, Corrosion Behaviour of Crystalline and Amorphous Forms of the Glass Forming Alloy Fe$_{43}$Cr$_{16}$ Mo$_{16}$C$_{15}$B$_{10}$, *J. Alloys Compd.*, 2012, **527**, p 210-218
5. J. Cheng, Z. Wang, and B. Xu, Wear and Corrosion Behaviors of FeCrBSiNbW Amorphous/Nanocrystalline Coating Prepared by Arc Spraying Process, *J. Therm. Spray Technol.*, 2012, **21**, p 1025-1031
6. X. Liu, Y. Zheng, X. Chang, W. Hou, J. Wang, Z. Tang, and A. Burgess, Microstructure and Properties of Fe-Based Amorphous Metallic Coating Produced by High Velocity Axial Plasma Spraying, *J. Alloys Compd.*, 2009, **484**, p 300-308
7. P. Suegama, C. Fugivara, A. Benedetti, J. Fernández, J. Delgado, and J. Guilemany, Electrochemical Behavior of Thermally Sprayed Stainless Steel Coatings in 3.4% NaCl Solution, *Corros. Sci.*, 2005, **47**, p 605-620
8. M. Verdian, K. Raeissi, and M. Salehi, Corrosion Performance of HVOF and APS Thermally Sprayed NiTi Intermetallic Coatings in 3.5% NaCl Solution, *Corros. Sci.*, 2010, **52**, p 1052-1059
9. B. Yilbas, I. Toor, F. Patel, and M. Baig, Effects of Laser Re-melting on the Corrosion Properties of HVOF Coatings, *J. Mater. Eng. Perform.*, 2013, **22**, p 1505-1511
10. S. Hong, Y. Wu, Q. Wang, G. Ying, G. Li, W. Gao, B. Wang, and W. Guo, Microstructure and Cavitation-Silt Erosion Behavior of High-Velocity Oxygen-Fuel (HVOF) Sprayed Cr$_3$C$_2$-NiCr Coating, *Surf. Coat. Technol.*, 2013, **225**, p 85-91
11. S. Hong, Y. Wu, Y. Zheng, B. Wang, W. Gao, G. Li, G. Ying, and J. Lin, Effect of Spray Parameters on the Corrosion Behavior of HVOF Sprayed WC-Co-Cr Coatings, *J. Mater. Eng. Perform.*, 2014, **23**, p 1434-1439
12. M. Verdian, K. Raeissi, and M. Salehi, Electrochemical Impedance Spectroscopy of HVOF-Sprayed NiTi Intermetallic Coatings Deposited on AISI, 1045 Steel, *J. Alloys Compd.*, 2010, **507**, p 42-46
13. J. Farmer, J. Haslam, S. Day, T. Lian, C. Saw, P. Hailey, J. Choi, R. Rebak, N. Yang, and J. Payer, Corrosion Resistance of Thermally Sprayed High-Boron Iron-Based Amorphous-Metal Coatings: Fe$_{49.7}$Cr$_{17.7}$Mn$_{1.9}$Mo$_{7.4}$W$_{1.6}$B$_{15.2}$C$_{3.8}$Si$_{2.4}$, *J. Mater. Res.*, 2007, **22**, p 2297-2311
14. Y. Wu, P. Lin, C. Chu, Z. Wang, M. Cao, and J. Hu, Cavitation Erosion Characteristics of a Fe-Cr-Si-B-Mn Coating Fabricated by High Velocity Oxy-Fuel (HVOF) Thermal Spray, *Mater. Lett.*, 2007, **61**, p 1867-1872
15. Y. Wu, P. Lin, Z. Wang, and G. Li, Microstructure and Microhardness Characterization of a Fe-Based Coating Deposited by High-Velocity Oxy-Fuel Thermal Spraying, *J. Alloys Compd.*, 2009, **481**, p 719-724
16. J. Farmer, J. Choi, C. Saw, J. Haslam, D. Day, P. Hailey, T. Lian, R. Rebak, J. Perepezko, and J. Payer, Iron-Based Amorphous Metals: High-Performance Corrosion-Resistant Material Development, *Metall. Mater. Trans. A*, 2009, **40**, p 1289-1305
17. R. Guo, C. Zhang, Q. Chen, Y. Yang, N. Li, and L. Liu, Study of Structure and Corrosion Resistance of Fe-Based Amorphous Coatings Prepared by HVAF and HVOF, *Corros. Sci.*, 2011, **53**, p 2351-2356
18. J. Picas, M. Punset, M.T. Baile, E. Martin, and A. Forn, Effect of Oxygen/Fuel Ratio on the In-flight Particle Parameters and Properties of HVOF WC-CoCr Coatings, *Surf. Coat. Technol.*, 2011, **205**, p 364-368
19. L. Zhao, M. Maurer, F. Fischer, R. Dicks, and E. Lugscheider, Influence of Spray Parameters on the Particle In-flight Properties and the Properties of HVOF Coating of WC-CoCr, *Wear*, 2004, **257**, p 41-46
20. J. Picas, E. Ruperez, M. Punset, and A. Forn, Influence of HVOF Spraying Parameters on the Corrosion Resistance of WC-CoCr Coatings in Strong Acidic Environment, *Surf. Coat. Technol.*, 2013, **225**, p 47-57

21. Z. Zhou, L. Wang, F. Wang, H. Zhang, Y. Liu, and S. Xu, Formation and Corrosion Behavior of Fe-Based Amorphous Metallic Coatings by HVOF Thermal Spraying, *Surf. Coat. Technol.*, 2009, **204**, p 563-570

22. Y. Wang, S. Jiang, Y. Zheng, W. Ke, W. Sun, X. Chang, W. Hou, and J. Wang, Effect of Processing Parameters on the Microstructures and Corrosion Behavior of High-Velocity Oxy-Fuel (HVOF) Sprayed Fe-Based Amorphous Metallic Coatings, *Mater. Corros.*, 2013, **64**, p 1-10

23. G. Taguchi, Introduction to Quality Engineering: Designing Quality into Products and Processes, 1986

24. X. Bie, J. Lu, Y. Wang, L. Gong, Q. Ma, and Z. Ye, Optimization of Parameters for Deposition of Ga-Doped ZnO Films by DC Reactive Magnetron Sputtering Using Taguchi Method, *Appl. Surf. Sci.*, 2011, **257**, p 6125-6128

25. M. Nalbant, H. Gökkaya, and G. Sur, Application of Taguchi Method in the Optimization of Cutting Parameters for Surface Roughness in Turning, *Mater. Des.*, 2007, **28**, p 1379-1385

26. Y. Wang, S. Jiang, Y. Zheng, W. Ke, W. Sun, and J. Wang, Effect of Porosity Sealing Treatments on the Corrosion Resistance of High-Velocity Oxy Fuel(HVOF)-Sprayed Fe-Based Amorphous Metallic Coatings, *Surf. Coat. Technol.*, 2011, **206**, p 1307-1318

27. D. Weng, P. Jokiel, A. Uebleis, and H. Bonhni, Corrosion and Protection Characteristics of Zinc and Manganese Phosphate Coatings, *Surf. Coat. Technol.*, 1996, **88**, p 147-156

28. S. Koksal, F. Ficici, R. Kayikci, and O. Savas, Experimental Optimization of Dry Sliding Wear Behavior of In Situ AlB$_2$/Al Composite Based on Taguchi's Method, *Mater. Des.*, 2012, **42**, p 124-130

29. L. Gil and M. Staia, Influence of HVOF Parameters on the Corrosion Resistance of NiWCrBSi Coatings, *Thin Solid Films*, 2002, **420**, p 446-454

30. O. Maranho, D. Rodrigues, M. Boccalini, Jr., and A. Sinatora, Influence of Parameters of the HVOF Thermal Spray Process on the Properties of Multicomponent White Cast Iron Coatings, *Surf. Coat. Technol.*, 2008, **202**, p 3494-3500

31. R. Li, Z. Li, J. Huang, P. Zhang, and Y. Zhu, Effect of Ni-to-Fe Ratio on Structure and Properties of Ni-Fe-B-Si-Nb Coatings Fabricated by Laser Processing, *Surf. Sci.*, 2011, **257**, p 3554-3557

32. R. Guo, C. Zhang, Y. Yang, Y. Peng, and L. Liu, Corrosion and Wear Resistance of a Fe-Based Amorphous Coating in Underground Environment, *Intermetallics*, 2012, **30**, p 94-99

33. Y. Yang, C. Zhang, Y. Peng, Y. Yu, and L. Liu, Effects of Crystallization on the Corrosion Resistance of Fe-Based Amorphous Coatings, *Corros. Sci.*, 2012, **59**, p 10-19

34. Y. Wang, Y. Zheng, W. Ke, W. Sun, and J. Wang, Corrosion of High-Velocity Oxy-Fuel (HVOF) Sprayed Iron-Based Amorphous Metallic Coatings for Marine Pump in Sodium Chloride Solutions, *Mater. Corros.*, 2012, **63**, p 685-694